SPECIAL ISSUE RESEARCH ARTICLE

WILEY

Field-stepped ultra-wideline NMR at up to 36 T: On the inequivalence between field and frequency stepping

Ivan Hung[1] | Adam R. Altenhof[1,2] | Robert W. Schurko[1,2] | David L. Bryce[3] |
Oc Hee Han[4] | Zhehong Gan[1]

[1]National High Magnetic Field Laboratory, Tallahassee, FL, 32310, USA

[2]Department of Chemistry and Biochemistry, Florida State University, Tallahassee, FL, 32306, USA

[3]Department of Chemistry and Biomolecular Sciences, University of Ottawa, Ottawa, Ontario, K1N 6N5, Canada

[4]Western Seoul Center, Korea Basic Science Institute, Seoul, 03759, South Korea

Correspondence
Robert Schurko and Zhehong Gan, National High Magnetic Field Laboratory, 1800 East Paul Dirac Drive, Tallahassee. FL 32310, USA.
Email: rschurko@fsu.edu; gan@magnet.fsu.edu

Abstract

Field-stepped NMR spectroscopy at up to 36 T using the series-connected hybrid (SCH) magnet at the U.S. National High Magnetic Field Laboratory is demonstrated for acquiring ultra-wideline powder spectra of nuclei with very large quadrupolar interactions. Historically, NMR evolved from the continuous-wave (*cw*) field-swept method in the early days to the pulsed Fourier-transform method in the modern era. Spectra acquired using field sweeping are generally considered to be equivalent to those acquired using the pulsed method. Here, it is shown that field-stepped wideline spectra of half-integer spin quadrupolar nuclei acquired using WURST/CPMG methods can be significantly different from those acquired with the frequency-stepped method commonly used with superconducting magnets. The inequivalence arises from magnetic field-dependent NMR interactions such as the anisotropic chemical shift and second-order quadrupolar interactions; the latter is often the main interaction leading to ultra-wideline powder patterns of half-integer spin quadrupolar nuclei. This inequivalence needs be taken into account to accurately and correctly determine the quadrupolar coupling and chemical shift parameters. A simulation protocol is developed for spectral fitting to facilitate analysis of field-stepped ultra-wideline NMR spectra acquired using powered magnets. A MATLAB program which implements this protocol is available on request.

KEYWORDS
field stepping, quadrupole nuclei, simulations, solid-state NMR, wideline

1 | INTRODUCTION

Approximately 73% of NMR-active nuclei in the Periodic Table have nuclear spin quantum numbers $S > 1/2$ and, hence, are subject to quadrupolar interactions that impact NMR spectra. Many of them are found in chemical and biological samples of interest, as well as materials such as nanoparticles, metal–organic frameworks, zeolites, and glasses. As such, solid-state NMR of quadrupolar nuclei is a powerful method for characterization of molecular structure and dynamics. By measuring the chemical shift (CS) and electric field gradient (EFG) tensor parameters, it is possible to probe the local electronic environments of atoms, their interactions with neighboring atoms, and longer-range structure; this is often enabled in part by comparison of experimental tensor parameters to those obtained from quantum chemical calculations [1].

In cases of large quadrupolar interactions, NMR spectroscopy of quadrupolar nuclei is generally more challenging than for $S = 1/2$ nuclei. Quadrupolar coupling constants (C_Q) can vary from a few kilohertz or less to megahertz, or even gigahertz. For the central-transition (CT; $+1/2 \leftrightarrow -1/2$) patterns of half-integer quadrupolar nuclei, for which first-order quadrupolar broadening is absent, the second-order broadening often dominates the pattern shape and breadth, hindering resolution of magnetically inequivalent sites. High magnetic fields can effectively reduce the broadening effects of the second-order quadrupolar interaction. This line narrowing, along with the enhanced polarization and higher resonance frequency, leads to dramatic enhancements in both spectral resolution and signal sensitivity [2–4]. These gains are especially important for many quadrupolar nuclei that exhibit poor sensitivity due to their low gyromagnetic ratios, low natural abundances, and large nuclear quadrupole moments [5–7]. The National High Magnetic Field Laboratory of the United States has built a series-connected hybrid (SCH) magnet that can reach fields up to 36 T (^{1}H resonance frequency higher than 1.5 GHz) [4]. Openly accessible to researchers worldwide, this magnet has demonstrated its resolution and sensitivity benefits for quadrupolar nuclei in a variety of samples since being commissioned [5, 8–18].

For second-order quadrupolar broadening smaller than the magic-angle spinning rate, innovative methods such as double rotation (DOR) [19], dynamic-angle spinning (DAS) [20], multiple-quantum magic-angle spinning (MQMAS) [21], and satellite-transition magic-angle spinning (STMAS) [22] have been developed to refocus the second-order quadrupolar broadening and obtain isotropic spectral resolution. For larger second-order quadrupolar broadening, static powder spectra are usually acquired at multiple fields, and the EFG and CSA parameters are extracted from fitting and deconvolution. In this work, we focus on solid-state NMR of nuclei that possess very large quadrupolar interactions due to their large quadrupole moments and asymmetric electronic environments. Even with the reduced second-order quadrupolar broadening at high magnetic fields near 36 T, their CT spectra can still be over several megahertz wide, far beyond the achievable *rf* excitation bandwidth of conventional NMR probes (these are referred to as ultra-wideline [UW] NMR spectra) [23–26]. The *rf* excitation bandwidth is inversely proportional to the pulse length, typically a few microseconds with high amplitude *rf* fields. It is worth noting that a spin-echo sequence is usually necessary to avoid the loss of short time-domain signals during the dead time. The overall spectral bandwidth is usually limited by the longer refocusing pulse, which has a bandwidth insufficient for uniform refocusing of isochromats from across the broad pattern. In addition, the sinc function excitation profile of a monochromatic pulse tends to attenuate the outer edges of the powder pattern. This pulse bandwidth issue has been largely overcome using chirped pulses. The most commonly used chirp pulse for acquiring UW NMR spectra is the WURST (Wideband Uniform-Rate-smooth-Truncation) shaped pulse [27], which is often used in conjunction with Carr-Purcell Meiboom-Gill (CPMG) [28, 29] multiple-echo acquisition (i.e., WURST/CPMG) [30]. In principle, the WURST pulse bandwidth is not limited by the *rf* field strength, as the effective pulse rotation angle from the frequency sweep can be compensated by longer pulses. In addition, the frequency profile of the WURST pulse is flatter than that of the sinc function of monochromatic pulses. In practice, the WURST bandwidth is still limited by the probe tuning circuit bandwidth, $\omega_0/2\pi Q$. Here, ω_0 is the angular Larmor resonance frequency, and Q is the quality factor of the resonant probe circuit. Considering a resonance frequency of $\omega_0/2\pi \approx 100$ MHz and $Q \approx 100$, the typical probe bandwidth would be ~1 MHz. One could detune the probe circuit to make the probe bandwidth wider; however, this is counterproductive in terms of NMR sensitivity and probe efficiency.

For powder patterns with breadths in excess of 1 MHz, acquisition of multiple spectra by stepping the transmitter frequency is necessary to cover the full powder pattern breadth [31]. An undistorted UW NMR powder pattern can be reconstructed from a skyline projection of all of the "frequency-stepped" spectra. This skyline spectrum can then be fit using simulations at a fixed field strength to extract NMR parameters. Such a frequency-stepped protocol has been commonly used for nearly all superconducting NMR magnets which have persistent magnetic fields [23, 24]. The only practical nuisance is that the probe needs to be retuned repeatedly when the transmitter frequency is stepped. Automated probe tuning and matching devices have become available on commercial NMR instruments to address this practical inconvenience [32]. In principle, it is possible to obtain a result that appears to be equivalent to frequency stepping by fixing the transmitter frequency and stepping the magnetic field instead [33–36]. In fact, during the early days of continuous-wave (*cw*) NMR, field sweeping was predominant, especially for the acquisition of broad spectra [37], because it was easier to sweep the magnetic field than the transmitter frequency, and retuning of the probe circuit is not required. The spectral width of the field-swept method is practically unlimited; however, it has largely been abandoned despite these advantages after the introduction of the more efficient and versatile

pulsed Fourier-transform method. In fact, most modern NMR systems no longer have field-sweeping accessories. Field sweeping remains in use for electron paramagnetic resonance (EPR), as typical spectra are usually too wide for pulsed methods. It has been proven that the NMR spectra obtained with *cw* field-swept experiments are the same as those obtained by the Fourier transform of pulsed time-domain signals [38]. Hence, the field- and frequency-stepped methods are generally considered equivalent, giving rise to the same spectra under the high field approximation.

Powered magnets can not only generate higher magnetic fields than superconducting magnets but also offer the alternative of stepping the field instead of the frequency, because such powered magnets are generally capable of quickly changing magnetic field. The field-stepped method for acquiring UW NMR spectra has been applied on a resistively powered 25 T magnet at the NHMFL [33]. For the newer 36 T SCH magnet, the field-stepped method is the only viable option, as probe access is restricted for safety reasons when the magnet is above $\sim$18 T. However, in comparing sub-spectra acquired with field-stepped and frequency-stepped (single field) UW NMR experiments, it was noticed that key spectral features are not in the same frequency positions. This discrepancy can cause problems in the reconstruction of the full powder pattern.

Herein, we present a study of the differences between the field- and frequency-stepped methods. As will be explained, the difference between the two methods stems from the magnetic field dependencies of anisotropic NMR interactions such as CS, and the first- and second-order quadrupolar interactions. The main objectives of this work are to develop a framework to understand this problem and to design a protocol for analysis of UW NMR spectra obtained using the field-stepped method on the highest-field NMR magnet available today. Experimental details regarding the operation of the unique SCH magnet and optimization of field-stepped WURST/CPMG experiments are also described.

2 | EXPERIMENTAL

The design and operation of the SCH magnet have been described previously [4]. Herein, the technical details relevant to performing field-stepped experiments are presented. For the SCH magnet, the resistive insert and superconducting outsert coils are connected in series. The large inductance of the outer superconducting coils helps to dampen the fast field fluctuations from the power supply. With the two magnets connected in

series, the current in the superconducting coil needs to be ramped simultaneously and rapidly with the resistive magnet. The superconducting coil is constructed via Cable-In-Conduit Conductor (CICC) with a vast number of bundled Nb_3Sn wires inside a stainless-steel pipe. Supercritical helium is pumped through the $\sim$30% void spaces inside the CICC to keep the Nb_3Sn wires in the superconducting state and, more importantly, to dissipate the heat generated from induced eddy currents inside the surrounding conventional conductor materials when ramping the current. The CICC construction enables the magnet to be ramped to the full 36 T field in about 30 min, at which point it runs with $\sim$20 kiloamps of current. At a ramp rate of 10 amps per second, it takes about a minute to change and settle each magnetic field step necessary to acquire UW NMR spectra.

The magnetic field of the SCH is regulated using a cascade flux and NMR control system. A magnetic flux pickup coil and external ^7Li NMR circuitry are installed for all NMR probes used on the SCH. A LiCl aqueous solution doped with 100 mM $MnCl_2$ provides a strong and fast relaxing ($T_1\sim$100 ms) ^7Li signal for field regulation. The paramagnetic doping is necessary because a duration of $\sim T_1$ is necessary for the *cw* NMR magnetization to reach a steady state. CS referencing of most nuclei is carried out by measuring the ^{17}O resonance frequency of a D_2O sample and calculating the IUPAC recommended reference frequencies [39]. When performing field-stepped measurements, the magnetic field can be regulated by adjusting the ^7Li lock frequency accordingly, but only within the frequency bandwidth of the ^7Li resonance circuit. When running unregulated, the magnetic field fluctuates within a range of about 20 ppm peak to peak, mostly from changes in the cooling water temperature. Thus, the overall line broadening from the field fluctuation is estimated to be $\sim$20 ppm when running unregulated. In addition, there is an initial field drift of about 100 ppm after ramping up the magnet, which settles down in $\sim$30–60 min after ramping to field. This initial period is often used to perform experimental calibrations and optimizations.

A ^1H/X double resonance static probe developed and built at the NHMFL was used for the UW NMR experiments. The probe uses an interchangeable coil platform with an outer loop-gap resonator for the ^1H channel and an inner solenoid coil for the X-nucleus. The solenoidal coil for a 4 mm cylindrical sample holder is $\sim$8 mm long.

For the WURST/CPMG experiments, identical excitation and refocusing pulses of equal *rf* field, length, sweep rate, and sweep range were used [30]. Such a condition was used for robustness to avoid modulations from the effective phase of the frequency sweep pulse rotation.

A "90°–180°" version of the WURST/CPMG sequence can give slightly more signal, though it requires a phase compensation between the excitation and refocusing pulses that depends on the *rf* amplitude, sweep range, and rate [40]. During the setup of WURST/CPMG, the WURST pulses were optimized for the broadest flat intensity profile in order to reduce the number of field steps and the total experimental time needed to acquire the complete UW NMR patterns. The sweep range was chosen to be close to the probe bandwidth until approximately 50% amplitude reflection at the two edges of the butterfly-shaped frequency sweep was observed on an oscilloscope through a directional coupler. For such wide sweep ranges, the effective *rf* field using a constant power is maximum at the center but attenuated at the edges. An overshoot of the *rf* field from the theoretical value [30] was used to compensate for the attenuation at the two edges, which yields a flatter intensity profile. In practice, we often observe a "tilt" in the intensity profile, which can be flattened by shifting the probe tuning slightly, while the reflected power is observed on the oscilloscope. Relatively flat, uniform profiles spanning ~1 MHz wide were obtained. It should be mentioned that even with these adjustments, small steps can still be observed at the edges of frequency sweeps, which should not be interpreted as real features of the UW NMR powder patterns.

Tetrachloroterephthalonitrile ($C_8Cl_4N_2$, 95% purity) and N-chlorosuccinimide ($C_4H_4ClNO_2$, 98% purity) were purchased from Sigma-Aldrich and used as received. Cs_4PbBr_6 and $CsPbBr_3$ crystal powder samples were prepared by slow temperature cooling from solution [41]. Samples were gently ground into fine powders and packed into sample holders for NMR experiments.

Simulations of field-stepped powder patterns were carried out in MATLAB [42] using custom routines implemented in a convenient graphical user interface (GUI) designed in our research group. Powder averaging was accomplished in the time domain with a Fibonacci series-based grid [43, 44]. The Hamiltonians, including the Zeeman, quadrupole, and CS interactions, were diagonalized, and the NMR transition frequencies were calculated over every orientation in the grid [45]. Such direct calculations take all higher-order quadrupolar interactions into account, which can become significant for large quadrupolar couplings. Numerical simulations in SIMPSON [46, 47] were used to verify non-ideal features and artifacts in the spectra arising from the overlap of isochromats associated with the central- and satellite-transitions (vide supra). All SIMPSON input files and the field-stepped simulation software package are available upon request.

3 | RESULTS AND DISCUSSION

The discrepancy between the field- and frequency-stepped methods was first noticed when comparing spectral features observed in the ^{35}Cl WURST/CPMG NMR sub-spectra of tetrachloroterephthalonitrile acquired with three consecutive field increments. Figure 1 shows two discontinuities arising from the overlap of two patterns corresponding to two crystallographically inequivalent sites with slightly different quadrupolar coupling constants [48]. The three sub-spectra were acquired with B_0 field increment steps of 0.096 T, which correspond to changes in Larmor frequency of 400 kHz. If the sub-spectra are shifted with respect to each other by 400 kHz to account for the difference in B_0 fields used during acquisition, the discontinuities corresponding to the two distinct ^{35}Cl sites do not align as would be expected if these spectra were acquired by stepping the frequency at a fixed B_0 field.

The origin of this problem comes from the field dependence of the spin interactions that contribute to the NMR frequency,

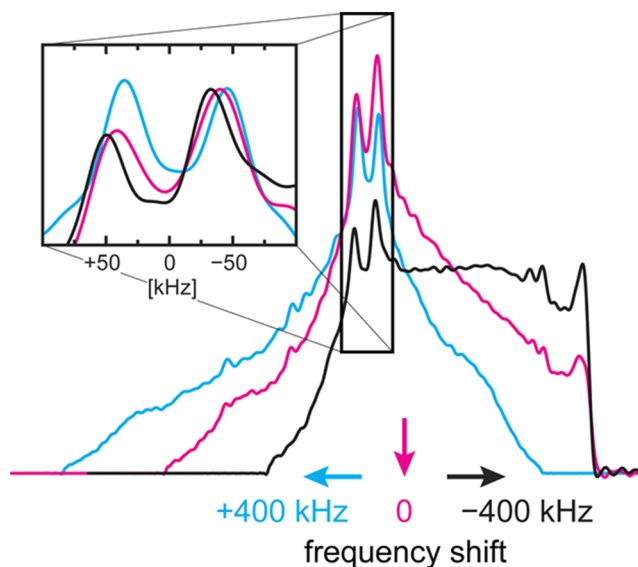$$\omega(B_0) = -\gamma B_0(1 + \delta) + Q_1 + \frac{Q_2}{\gamma B_0}. \tag{1}$$

FIGURE 1 ^{35}Cl WURST/CPMG NMR sub-spectra of tetrachloroterephthalonitrile showing that the spectral features for the two distinct sites in the sample do not align after the sub-spectra are shifted in frequency to correspond with the difference in magnetic fields used to acquire the sub-spectra. Inset shows an expansion of the two features, where the spectral intensities for the peak on the right have been normalized to aid visual comparison

Here, δ is the CS; the first-order quadrupolar interaction Q_1 is field independent; $Q_2/\gamma B_0$ represents the second-order quadrupolar interaction, which is inversely proportional to the field, and most often the primary term of interest for UW NMR. Other possible smaller interactions such as higher-order quadrupolar interactions, the field-independent J and dipolar couplings, and the quadratic magnetically induced alignment term are not considered in Equation 1. When acquiring spectra at two different fields, B_0 and $B_0 + \Delta B$, where ΔB is the change in field, the NMR signal appears at different positions relative to the same carrier frequency. One obtains the following difference in peak positions $\Delta\omega$ from Equation 1:

$$\Delta\omega \approx -\gamma\Delta B\left(1 + \delta + \frac{Q_2}{\gamma^2 B_0^2}\right). \quad (2)$$

The term representing the change of Larmor frequency $-\gamma\Delta B$ can be taken into account by shifting the frequency axis. The remaining $-\gamma\Delta B\left(\delta + \frac{Q_2}{\gamma^2 B_0^2}\right)$ term represents the inequivalence between the field- and frequency-stepped methods. With the large field increments enabled by the large bandwidth of WURST/CPMG experiments, sizable differences in peak positions can arise, and an inequivalence between the field- and frequency-stepped methods can be observed for samples with large anisotropic CSs and second-order quadrupolar broadenings as illustrated in Figure 1. It should be noted that the equivalence between the field- and frequency-stepped methods remains intact when the first-order quadrupole coupling is the dominant broadening mechanism.

Figure 2 shows a complete set of field-stepped WURST/CPMG ^{35}Cl NMR sub-spectra for N-chlorosuccinimide. At each field, the WURST/CPMG experiment covers only an ~1 MHz segment of the UW NMR powder pattern. The powder pattern at each field is simulated and then multiplied by the WURST intensity profile. Both the experimental and simulated sub-spectra are frequency shifted with respect to the Larmor frequency at the central B_0 field ($B_0 = 34.42$ T) and plotted in Figure 2a for comparison. This procedure is somewhat cumbersome, but it follows directly from the field-stepped acquisition and, thus, takes into account all field-dependent effects. In order to cover the whole powder pattern, skyline projections of both the experimental and simulated sub-spectra can be constructed and compared, as shown in Figure 2b,c, respectively. This is the procedure we have adopted for fitting field-stepped UW NMR spectra. Powder line shapes are usually fit based on the position of distinct spectral features rather than by using the mean squared error. In this case with $\eta_Q \sim 0$, the
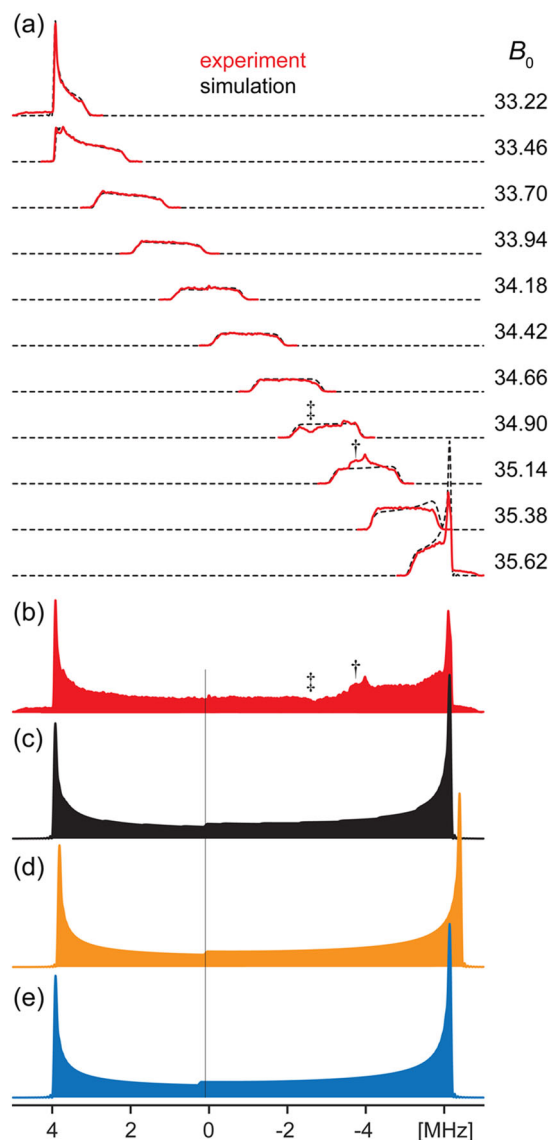

FIGURE 2 (a) Experimental (solid red traces) and simulated (dashed black traces) data of the field-stepped ^{35}Cl WURST/CPMG NMR sub-spectra for N-chlorosuccinimide. B_0 increments correspond to changes in Larmor frequency $\Delta\nu_0(^{35}\text{Cl})$ of ±1.0 MHz. Skyline projections of the (b) experimental and (c) simulated sub-spectra shown in (a). (d) Simulation at the center B_0 field value, $B_0 = 34.42$ T, using the best fit parameters ($\delta_{iso} = 625$ ppm, $C_Q = 106.7$ MHz, $\eta_Q = 0$) obtained from simulation of the field-stepped sub-spectra. (e) A simulated fit of the experimental projection in (a) at the center field yields erroneous NMR parameters ($\delta_{iso} = 1{,}725$ ppm, $C_Q = 106.0$ MHz, $\eta_Q = 0$), which leads to a major discrepancy in the location of the feature located near the center of the powder pattern, which is highlighted by the vertical line crossing through the spectra in (b) to (e). † denotes signal arising from the high frequency ^{37}Cl ST, and ‡ denotes a systematic depletion in the spectrum as a result of overlap between the ^{35}Cl ST and CT frequencies (see details in the text)

features of interest are the two peaks at the edges and a small step near the central field.

To illustrate the extent of the inequivalence between the field- and frequency-stepped methods, Figure 2d shows a simulation of the full powder pattern at the central B_0 field using the quadrupole coupling parameters obtained from the field-stepped simulations above. The comparison with the field-stepped method shows significant differences in the positions of the two edges. This is not surprising because these sub-spectra were acquired with large field differences ΔB with respect to the center field. If the complete pattern is fit at a single B_0 field, significant errors result including a CS toward lower field by over a thousand ppm and a reduction in the quadrupolar coupling by 0.7 MHz (Figure 2e). The fitting would also shift the small step in the middle out of position with respect to the experimental powder pattern. This example demonstrates the extent to which the field- and frequency-stepped methods are inequivalent. It also shows that this inequivalence needs be taken into account in order to measure the quadrupole coupling and CS parameters properly.

Figure 2 also shows two distinct features in the experimental powder pattern between −2 and −4 MHz marked by the † and ‡ symbols that are absent in the simulations. The former is signal arising from the ST of the other isotope of chlorine, ^{37}Cl, recognized first by using the QUEST [49] simulation program and later included in the field-stepped simulation protocol. The latter is a depletion of signal arising from overlap with ^{35}Cl ST frequencies (vide infra). In addition, small regular steps in intensity are noticeable in the simulations at the edges of

WURST frequency sweeps. These steps are more obvious in the simulated spectrum than the experimental one, where they are obscured by the noise and should not be interpreted as spectral features.

Can the inequivalence between field and frequency stepping be corrected by simply adjusting the frequency axis? This is possible when there is only one pattern arising from a magnetically distinct single site, and the field value at zero CS is known. Equation 2 shows that the sign and magnitude of the field-stepped effect vary with the second-order quadrupolar shift and can become complicated further when the CS anisotropy becomes large and needs to be considered. It is not practical to compensate for these effects by scaling the frequency axis without prior knowledge of the quadrupolar parameters and CS anisotropy, particularly if there are patterns arising from multiple magnetically and/or chemically distinct sites.

Figure 3a shows a field-stepped ^{79}Br UW NMR spectrum of Cs_4PbBr_6, which was acquired using four B_0 increments. The experimental spectrum exhibits augmented intensity in the discontinuities of the powder pattern, but this does not hinder the fitting routine. The fitting is executed as described above and yields the quadrupolar parameters noted in the figure. The ^{79}Br UW NMR spectrum of $CsPbBr_3$ was acquired with seven B_0 increments due to its much larger C_Q (Figure 3b) and simulated in a similar manner. Two unique features appear in this powder pattern, much like the ^{35}Cl example, originating from ^{81}Br ST signal (†) and a signal depletion due to overlap with ^{79}Br STs (‡, vide infra).
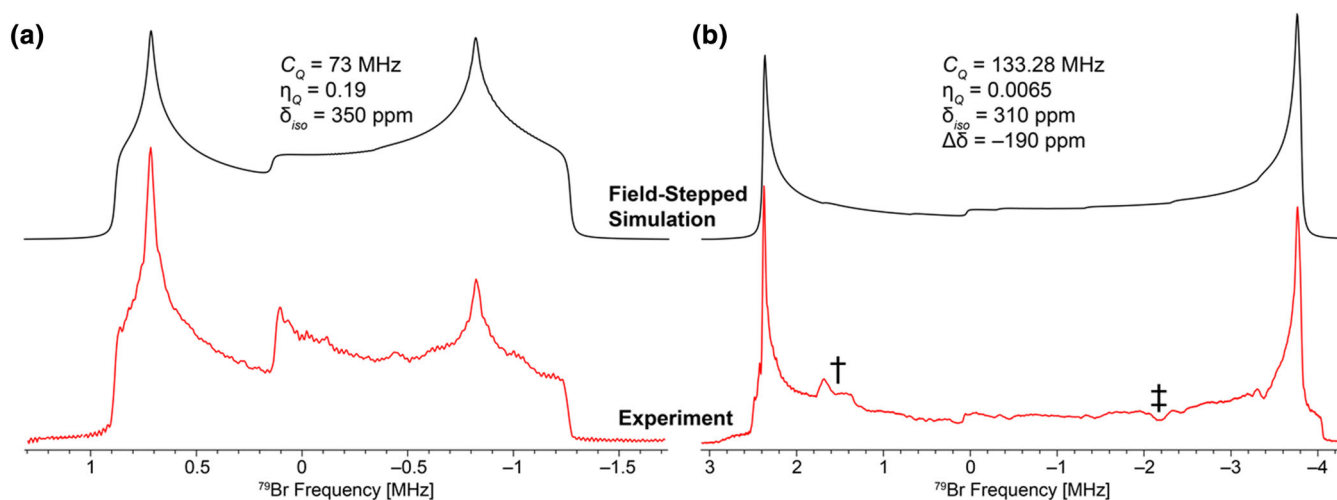

FIGURE 3 Experimental (bottom row) and simulated (top row) ^{79}Br NMR spectra of zero-dimensional perovskites [41] (a) Cs_4PbBr_6 and (b) $CsPbBr_3$. Spectra in (a) were acquired with four B_0 increments corresponding to $\Delta\nu_0(^{79}Br) = \pm0.5$ MHz between each sub-spectrum. Spectra in (b) were acquired with seven B_0 increments corresponding $\Delta\nu_0(^{79}Br) = \pm1.0$ MHz between each sub-spectrum. All spectra are referenced to a central Larmor frequency of $\nu_0(^{79}Br) = 375.810$ MHz at $B_0 = 35.23$ T. The WURST sweep width is $\Delta\nu = 2.0$ MHz in every case. † denotes signal arising from ^{81}Br STs. ‡ denotes a systematic depletion of signal intensities where the ST and CT frequency overlap (see details in the text)

In the experimental ^{35}Cl and ^{79}Br UW NMR spectra (Figures 2 and 3), two types of spectral features/artifacts are observed. First is the overlap of the ^{35}Cl/^{79}Br CT signals with ^{37}Cl/^{81}Br ST signals (denoted by †). This can manifest itself for common NMR-active isotope pairs with similar gyromagnetic ratios, such as $^{35/37}$Cl, $^{47/49}$Ti, $^{63/65}$Cu, $^{79/81}$Br, $^{113/115}$In, and $^{185/187}$Re [49]. Second is a depletion of signal that is known to occur in UW NMR of CT powder patterns (denoted by ‡). This originates from a subset of isochromats associated with both the CT and ST patterns of the same nucleus with similar resonance frequencies that are within the WURST sweep width. For these isochromats, the *rf* irradiation is no longer selective for the CT, causing not only coherence transfer and leakage from the CT to other transitions but also changes in the effective *rf* nutation frequency of the WURST pulses, both of which contribute to signal depletion [50]. This artifact is more pronounced when the EFG tensor is close to axial symmetry with its largest component at or near the magic angle (i.e., the angle between the largest component of the EFG tensor V_{33} and B_0 is $\beta^{EFG} \approx 54.74°$), similar to the "magic-angle hole" effect in cross-polarization spectra. For samples with asymmetric EFG tensors, the signal depletion still occurs but is less noticeable because isochromats with β^{EFG} near the magic angle are spread across the powder patterns.

The ^{35}Cl powder pattern in Figure 2 was simulated with the inclusion of the high frequency ^{37}Cl ST (Figure 4b), confirming the origin of the feature at approximately −4 MHz. A numerical simulation in SIMPSON [46] was conducted using WURST/CPMG pulse sequence parameters that are identical to those used for the experimental acquisition (Figure 4c), in order to model the overlap between the ^{35}Cl CT and ST patterns for the $\beta^{EFG} \approx 54.74°$ isochromats. The full quantum mechanical simulation shows a depletion of signal intensity that matches well with what is observed experimentally and agrees with previous observations for CT powder patterns acquired with WURST/CPMG [50, 51]. The ^{79}Br powder pattern in Figure 3b was also simulated by including a ^{81}Br ST pattern (Figure 4e), revealing a similarly good match with the experimental feature at approximately +1.6 MHz. The characteristic depletion of signal for the $\beta^{EFG} \approx 54.74°$ isochromats was also simulated using SIMPSON, and the two ^{79}Br sub-spectra show a very similar depletion at the same resonance (Figure 4f). It is important to note that it is not necessary to simulate this depletion of signal in order to accurately extract the quadrupolar parameters, especially because numerical simulations with large powder grids are necessary in this case, which is computationally expensive. However, we modeled the signal depletion to demonstrate that this feature is a general characteristic of UW NMR CT spectra with near axial EFG tensors.

It is beneficial to identify, understand, and simulate the extra features shown above. For instance, the ^{37}Cl ST in Figure 4a clearly shows a line shape which is inconsistent with a strictly axial EFG tensor; that is, η_Q is not exactly equal to 0. The line shape effect on the much larger first-order quadrupole interaction allows for an accurate determination of $\eta_Q = 0.0093 \pm 0.0002$ for the ^{37}Cl quadrupole coupling tensor of N-chlorosuccinimide. The quadrupolar coupling constants are different for the two isotopes of chlorine because of their different
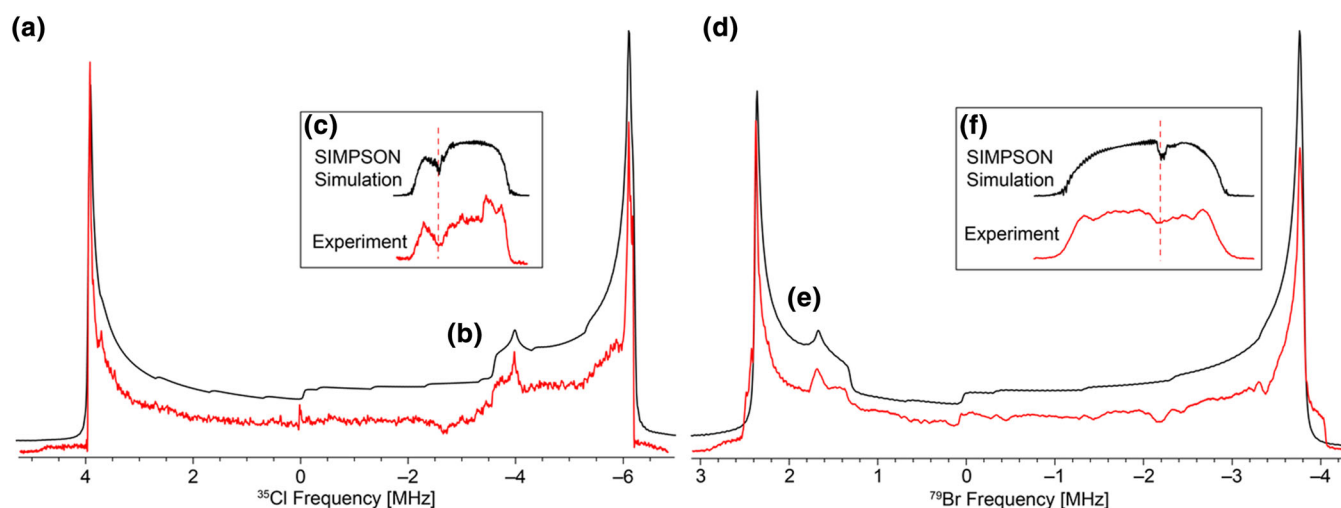

FIGURE 4 (a) Experimental ^{35}Cl field-stepped NMR spectrum of N-chlorosuccinimide, (b) a field-stepped simulation of (a) that includes the high-frequency ^{37}Cl ST spectrum, and (c) a numerical SIMPSON simulation of the sub-spectrum that was experimentally acquired at $B_0 = 34.90$ T. (d) Experimental ^{79}Br NMR spectrum of CsPbBr$_3$, (e) a field stepped simulation of (d) that includes the low-frequency ^{81}Br spectrum, and (f) a numerical SIMPSON simulation of the sub-spectrum that was experimentally acquired at $B_0 = 35.05$ T

quadrupole moments, but the asymmetry parameters of their respective EFG tensors are the same. In addition to the shape of the ^{37}Cl ST, its position also provides significant constraints to determining C_Q. In order to properly fit the features of the ^{35}Cl CT pattern (i.e., the two "horns" and small step-like feature in the middle), it seems necessary in the present case to include an axially symmetric CS tensor with an anisotropy of $\delta_\sigma \approx -850$ ppm, with the major components of the EFG and CS tensors coincident with one another. Determining CSA can be challenging for UW NMR spectra, which are usually dominated by the second-order quadrupolar broadening. Nevertheless, high magnetic fields can aid in accurate measurement of CS tensor parameters, because the effects of CSA scale proportionally to the strength of B_0. The differences between the field- and frequency-stepped methods must be taken into account in order to accurately measure relatively small CSAs, even for UW NMR patterns acquired at up to 36 T.

In order to be able to rapidly simulate field-stepped UW NMR spectra, we wrote a program in MATLAB that is implemented with a GUI that is convenient for end-users (Figure 5). Experimental spectra can be loaded into the spectral window and overlayed with the simulation for fitting. The program requires the installation of MATLAB and its parallel computing toolbox (this code can be obtained by contacting the authors).

4 | CONCLUSION

In summary, it has been shown that field-stepped experiments can be carried out quickly using the 36 T Series-Connected-Hybrid magnet at the NHMFL for UW NMR of quadrupolar nuclei, providing unprecedented resolution and sensitivity. The field dependences of the second-order quadrupolar coupling and CSA cause inequivalences between spectra acquired using the field-stepped and commonly used frequency-stepped methods, which can lead to significant errors in the determination of quadrupolar coupling and CS parameters. As illustrated with ^{35}Cl and ^{79}Br UW NMR spectra as examples, a spectral simulation and fitting protocol that takes the field dependence into account was developed for UW
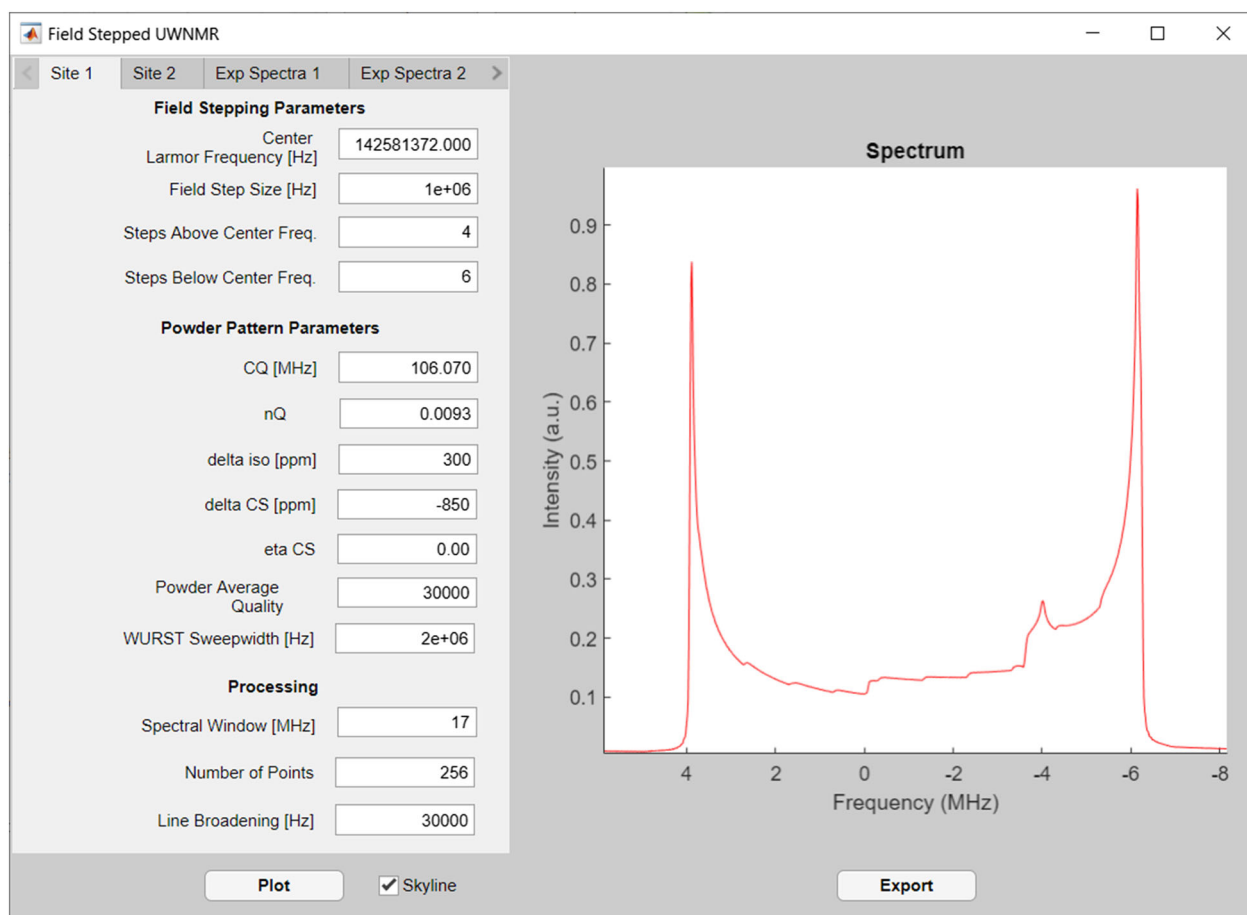

FIGURE 5 A screen shot of the field-stepped simulation software implemented in MATLAB. A simulation of the ^{35}Cl powder pattern shown in Figure 4 is displayed with all of the input parameters used for its generation

NMR applications using the highest field NMR magnet available today. The use of this protocol is demonstrated to be crucial for the accurate measurement of large C_Q values, quadrupolar asymmetry parameters, and CSAs from UW NMR patterns of quadrupolar nuclei acquired at very high fields.

PEER REVIEW

The peer review history for this article is available at https://publons.com/publon/10.1002/mrc.5128.

ORCID

Ivan Hung https://orcid.org/0000-0001-8916-739X
Zhehong Gan https://orcid.org/0000-0002-9855-5113

REFERENCES

[1] D. L. Bryce, *IUCrJ* **2017**, *4*, 350.

[2] Z. Gan, P. Gor'kov, T. A. Cross, A. Samoson, D. Massiot, *J. Am. Chem. Soc.* **2002**, *124*, 5634.

[3] M. K. Pandey, K. Hashi, S. Ohki, G. Nishijima, S. Matsumoto, T. Noguchi, K. Deguchi, A. Goto, T. Shimizu, H. Maeda, *Anal. Sci.* **2016**, *32*, 1339.

[4] Z. Gan, I. Hung, X. Wang, J. Paulino, G. Wu, I. M. Litvak, P. L. Gor'kov, W. W. Brey, P. Lendi, J. L. Schiano, M. D. Bird, I. R. Dixon, J. Toth, G. S. Boebinger, T. A. Cross, *J. Magn. Reson.* **2017**, *284*, 125.

[5] C. Bonhomme, X. Wang, I. Hung, Z. Gan, C. Gervais, C. Sassoye, J. Rimsza, J. Du, M. E. Smith, J. V. Hanna, S. Sarda, P. Gras, C. Combes, D. Laurencin, *Chem. Commun.* **2018**, *54*, 9591.

[6] P. J. Sideris, U. G. Nielsen, Z. Gan, C. P. Grey, *Science* **2008**, *321*, 113.

[7] K. M. N. Burgess, F. A. Perras, I. L. Moudrakovski, Y. Xu, D. L. Bryce, *Can. J. Chem.* **2015**, *93*, 799.

[8] J. Paulino, M. Yi, I. Hung, Z. Gan, X. Wang, E. Y. Chekmenev, H.-X. Zhou, T. A. Cross, *PNAS* **2020**, *117*, 11908.

[9] R. S. Madsen, A. Qiao, J. Sen, I. Hung, K. Chen, Z. Gan, S. Sen, Y. Yue, *Science* **2020**, *367*, 1473.

[10] S. E. Ashbrook, D. M. Dawson, Z. Gan, J. E. Hooper, I. Hung, L. E. Macfarlane, D. McKay, L. K. McLeod, R. I. Walton, *Inorg. Chem.* **2020**, *59*, 11616.

[11] V. Martins, J. Xu, X. Wang, K. Chen, I. Hung, Z. Gan, C. Gervais, C. Bonhomme, S. Jiang, A. Zheng, B. E. G. Lucier, Y. Huang, *J. Am. Chem. Soc.* **2020**, *142*, 14877.

[12] E. G. Keeler, V. K. Michaelis, C. B. Wilson, I. Hung, X. Wang, Z. Gan, R. G. Griffin, *J. Phys. Chem. B* **2019**, *123*, 3061.

[13] E. G. Keeler, V. K. Michaelis, M. T. Colvin, I. Hung, P. L. Gor'kov, T. A. Cross, Z. Gan, R. G. Griffin, *J. Am. Chem. Soc.* **2017**, *139*, 17953.

[14] L. Shen, Y. Wang, J.-H. Du, K. Chen, Z. Lin, Y. Wen, I. Hung, Z. Gan, L. Peng, *ChemCatChem* **2020**, *12*, 1569.

[15] Q. Wang, W. Li, I. Hung, F. Mentink-Vigier, X. Wang, G. Qi, X. Wang, Z. Gan, J. Xu, F. Deng, *Nat. Commun.* **2020**, *11*, 3620.

[16] J. Shen, V. Terskikh, X. Wang, I. Hung, Z. Gan, G. Wu, *J. Phys. Chem. B* **2018**, *122*, 4813.

[17] C.-H. Chen, E. Gaillard, F. Mentink-Vigier, K. Chen, Z. Gan, P. Gaveau, B. Rebiere, R. Berthelot, P. Florian, C. Bonhomme, M. E. Smith, T.-X. Metro, B. Alonso, D. Laurencin, *Inorg. Chem.*, *asap.* **2020**, *59*, 13050. https://doi.org/10.1021/acs.inorgchem.0c00208

[18] P. M. J. Szell, D. L. Bryce, *Concepts Magn. Reson. Part A* **2016**, *45A*, e21412.

[19] A. Samoson, E. Lippmaa, A. Pines, *Mol. Phys.* **1988**, *65*, 1013.

[20] K. T. Mueller, B. Q. Sun, G. C. Chingas, J. W. Zwanziger, T. Terao, A. Pines, *J. Magn. Reson.* **1990**, *86*, 470.

[21] L. Frydman, J. S. Harwood, *J. Am. Chem. Soc.* **1995**, *117*, 5367.

[22] Z. H. Gan, *J. Am. Chem. Soc.* **2000**, *122*, 3242.

[23] D. L. Bryce, *Dalton Trans.* **2019**, *48*, 8014.

[24] R. W. Schurko, *Acc. Chem. Res.* **2013**, *46*, 1985.

[25] R. W. Schurko, in *EMagRes*, American Cancer Society, **2011**.

[26] A. R. Altenhof, M. J. Jaroszewicz, A. W. Lindquist, L. D. D. Foster, S. L. Veinberg, R. W. Schurko, *J. Phys. Chem. C* **2020**, *124*, 14730.

[27] E. Kupce, R. Freeman, *J. Magn. Reson., Ser. A* **1995**, *115*, 273.

[28] H. Y. Carr, E. M. Purcell, *Phys. Rev.* **1954**, *94*, 630.

[29] S. Meiboom, D. Gill, *Rev. Sci. Instrum.* **1958**, *29*, 688.

[30] L. A. O'Dell, A. J. Rossini, R. W. Schurko, *Chem. Phys. Lett.* **2009**, *468*, 330.

[31] D. Massiot, I. Farnan, N. Gautier, D. Trumeau, P. Florian, P. Grandinetti, *J. Chim. Phys.-Chim. Biol.* **1995**, *92*, 1847.

[32] O. Pecher, D. M. Halat, J. Lee, Z. Liu, K. J. Griffith, M. Braun, C. P. Grey, *J. Magn. Reson.* **2017**, *275*, 127.

[33] I. Hung, K. Shetty, P. D. Ellis, W. W. Brey, Z. Gan, *Solid State Nucl. Magn. Reson.* **2009**, *36*, 159.

[34] K. Yamada, *Bull. Chem. Soc. Jpn.* **2017**, *90*, 1224.

[35] C. A. Klug, J. B. Miller, *Solid State Nucl. Magn. Reson.* **2018**, *92*, 14.

[36] K. Yamada, T. Yamaguchi, R. Ohashi, S. Ohki, K. Deguchi, K. Hashi, A. Goto, T. Shimizu, *Solid State Nucl. Magn. Reson.* **2020**, *109*, 101688.

[37] A. Abragam, *The Principles of Nuclear Magnetism*, Clarendon Press **1961**.

[38] R. R. Ernst, G. Bodenhausen, A. Wokaun, *Principles of Nuclear Magnetic Resonance in One and Two Dimensions*, Oxford University Press, New York **1987**.

[39] R. K. Harris, E. D. Becker, S. M. C. De Menezes, R. Goodfellow, P. Granger, *Pure Appl. Chem.* **2001**, *73*, 1795.

[40] I. Hung, Z. Gan, *J. Magn. Reson.* **2010**, *204*, 256.

[41] J.-H. Cha, H.-J. Lee, S. H. Kim, K. C. Ko, B. J. Suh, O. H. Han, D.-Y. Jung, *ACS Energy Lett.* **2020**, *5*, 2208.

[42] MATLAB, Version 8.4.0.150421 (R2014b), The MathWorks Inc., Natick, Massachusetts, **2014**.

[43] Á. González, *Mathematical Geosciences* **2010**, *42*, 49.

[44] C. Crăciun, *J. Magn. Reson.* **2014**, *245*, 63.

[45] F. A. Perras, D. L. Bryce, *Angew. Chem.-Int. Edit.* **2012**, *51*, 4227.

[46] M. Bak, J. T. Rasmussen, N. C. Nielsen, *J. Magn. Reson.* **2000**, *147*, 296.

[47] Z. Tošner, R. Andersen, B. Stevensson, M. Edén, N. C. Nielsen, T. Vosegaard, *J. Magn. Reson.* **2014**, *246*, 79.

[48] P. M. J. Szell, D. L. Bryce, *The Journal of Physical Chemistry C* **2016**, *120*, 11121.

[49] F. A. Perras, C. M. Widdifield, D. L. Bryce, *Solid State Nucl. Magn. Reson.* **2012**, *46*, 36.

[50] J. Koppe, M. R. Hansen, *J. Phys. Chem. A* **2020**, *124*, 4314.

[51] A. R. Altenhof, A. W. Lindquist, L. D. D. Foster, S. T. Holmes, R. W. Schurko, *J. Magn. Reson.* **2019**, *309*, 106612.